Key Points:
- New approach has been developed to empirically model the magnetospheric magnetic field, based on a synthesis of the modular and RBF methods
- Combines strengths and minimizes weaknesses of both above methods, as demonstrated by the data-based modeling of four storm phases
- Allows to faithfully represent contributions to the total field from all major sources such as the tail, ring, Birkeland, and cusp currents

Correspondence to:
N. A. Tsyganenko,
n.tsyganenko@spbu.ru

A hybrid approach to empirical magnetosphere modeling

N. A. Tsyganenko[1] [ID] and V. A. Andreeva[1] [ID]

[1]Institute and Department of Physics, Saint Petersburg State University, Saint Petersburg, Russia

Abstract A new approach has been devised and explored to reconstruct magnetospheric configurations, based on spacecraft data and a synthesis of two methods of modeling the magnetic field of extraterrestrial currents. The main idea is to combine within a single framework (1) a modular structure explicitly representing separate contributions to the total field from the magnetopause, ring, tail, and field-aligned currents, and (2) a system of densely distributed field sources, modeled by the radial basis functions (RBF). In such an arrangement, the modular part takes on a role of the principal component representing the gross large-scale structure of the magnetosphere, whereas the RBF part serves as a higher-order correction that compensates for the lack of flexibility of the modular component. The approach has been tested on four subsets of spacecraft data, corresponding to four phases of a geomagnetic storm, and was shown to tangibly improve the model's performance. In particular, it allows proper representation of magnetic effects of the field-aligned currents both at low altitudes and in the distant magnetosphere, as well as inclusion of extensive high-latitude field depressions associated with diamagnetism of the polar cusp plasma, missing in earlier empirical models. It also helps to more accurately model the nightside magnetosphere, so that most of the large-scale magnetotail field is compactly described by a dedicated module inherited from an earlier empirical model, while the RBF component's task is to resolve finer details in the inner magnetosphere.

1. Introduction

In our recent publications [*Andreeva and Tsyganenko*, 2016; *Tsyganenko and Andreeva*, 2016, henceforth AT16 and TA16, respectively], a new approach was presented to empirically model the magnetospheric magnetic field, which does not impose preconceived a priori restrictions on the field source geometry and makes it easy to control and vary the model's spatial resolution. The approach is based on representing the model field in terms of toroidal and poloidal components, whose generating potentials are expanded into a set of radial basis functions (RBF). The RBF nodes are more or less evenly distributed over the modeling region, and the corresponding magnitude coefficients are derived from large sets of spacecraft data. It was shown that, due to high flexibility of the mathematical framework, the obtained models can faithfully extract from data even fine details of the magnetospheric field structure that previously remained beyond the reach of the standard modular approach.

These advantages notwithstanding, the new RBF method has certain weaknesses, of which the foremost relates to the very wide range of spatial scales of the magnetospheric current systems. Thus, the transverse scale of the field-aligned currents (FACs) varies from $100-300$ km at low altitudes up to as large as a few R_E in the distant magnetosphere. An immediate consequence of this fact is that, in order to faithfully reconstruct the magnetic effects of the low-altitude FACs, one would have to densely cover the innermost region $1 \leq r \leq 3\,R_E$ with the RBF nodes (AT16, section 6). Unfortunately, any attempts to smoothly extend the fine inner grid to larger distances and thus construct a global RBF meshwork with a decent resolution would inevitably result in a computationally prohibitive number of the nodes.

The goal of the present paper is to describe an efficient way to mitigate the problem, based on the idea that the gross global structure of the magnetosphere can be fairly well represented by a standard modular model of the kind developed in our past works [reviewed in *Tsyganenko*, 2013], while the remaining inaccuracies can be removed by adding an RBF component to the base modular model. More specifically, it is suggested to describe the principal contribution from the magnetopause currents, the symmetric and partial ring currents, the magnetotail current sheet, and the FACs by means of flexible "prefabricated" modules inherited from our recent data-based model [*Tsyganenko and Andreeva*, 2015; henceforth TA15]. Then the role of the

RBF component, added on top of the modular one, is to serve as a higher-order correction to the modular part. In particular, in the TA15 model the Region 1 FACs were assumed to form relatively thin "curtains," aligned with quasi-dipolar magnetic field lines at low altitudes and smoothly deflected toward higher latitudes at larger distances. Due to lack of knowledge of the actual configuration of the distant FACs, it was further supposed in TA15 that, while diverging outward, the FAC flow lines stayed in the same solar magnetic (SM) meridian planes at all distances. In the proposed hybrid approach, adding the RBF field to the modular component lifts that artificial assumption and allows the distant FACs to flexibly adjust their global geometry to the data.

Another improvement made possible due to the inclusion of the RBF component concerns the diamagnetic effect of the cusp currents. The extensive magnetic depressions caused by the injected magnetosheath particles were discussed in many publications since their detection in early observations [e.g., *Farrell and Van Allen*, 1990; *Fairfield*, 1991; *Tsyganenko*, 2009]. The routinely used data-based models, however, can reproduce only the "vacuum" component of the depression, associated with diverging field lines and null B points at the shielding boundary [*Tsyganenko and Russell*, 1999]. The RBF approach not only reveals the diamagnetic depression inside the model cusps, but also replicates the seasonal/diurnal asymmetry between the northern and southern cusps, associated with the dipole tilt (see, e.g., Figure 7 in AT16 and Figure 6 in TA16).

This paper consists of six sections. Section 2 overviews the hybrid model architecture and concisely recapitulates in separate subsections 2.1 and 2.2 essential features of both the modular and the RBF components, presented earlier in detail in TA15, AT16, and TA16. At the end of the section, a brief description is also given of the hybrid fitting procedure. Section 3 overviews the modeling data set, and the missions the data came from, and provides details of data selection into subsets, corresponding to different magnetospheric states. Section 4 presents the main results of fitting the hybrid model to data and illustrates them with plots of equatorial and meridional field/current distributions. In section 5 we discuss the model field properties and evaluate the effect of adding the RBF component, in particular, in terms of the field line mapping. Section 6 summarizes the paper and outlines issues to be addressed in future developments.

2. The Model Architecture and Essence of the Fitting Procedure

As already said, the hybrid model is conceived as a synthesis of two components: the principal (modular) one, based on the TA15 modules, and the RBF component. Both components were separately described in detail in our earlier publications cited in section 1, for which reason only a concise outline of their structure is given below, to refresh the reader on the main principles. We first overview the modular component of the model in the next section 2.1.

2.1. Modular Component of the Hybrid Model

The modular component includes contributions from the following sources: (1) Chapman-Ferraro currents flowing on the magnetopause and shielding the Earth's dipole field outside the boundary, (2) the magnetotail current sheet, (3) the ring current (RC), including the symmetric (SRC) and the partial (PRC) component with its associated field-aligned (Region 2) currents, and (4) Region 1 FACs. Each intramagnetospheric module (2)–(4) is provided with its own shielding field, derived by minimizing the total normal field component at the model magnetopause, represented by a simplified version of the *Lin et al.* [2010] boundary. More details are given below of each of the above mentioned modules.

2.1.1. Dipole Shielding Field

Being associated with the Chapman-Ferraro currents at the magnetopause, the dipole shielding field $\mathbf{B}_{cf}$ is curl free everywhere inside the magnetosphere and, hence, is represented by the gradient of a scalar potential U_{cf}, which in turn is split into a linear combination

$$U_{cf} = U_\perp \cos \Psi + U_\parallel \sin \Psi \tag{1}$$

where Ψ is the Earth's dipole tilt angle, and the partial potentials $U_\perp$ and $U_\parallel$ correspond, respectively, to strictly perpendicular and parallel orientation of the dipole axis with respect to the solar wind direction. The most convenient and universally accepted form of the partial potentials in all recent models is the so-called "box" harmonic expansions

$$U_\perp = \sum_{i,k=1}^{N} a_{ik} \exp\left[x \sqrt{p_i^2 + p_k^2}\right] \cos(p_i y) \sin(p_k z) \tag{2}$$

$$U_\parallel = \sum_{i,k=1}^{N} b_{ik} \exp\left[x\sqrt{q_i^2 + q_k^2} \right] \cos(q_i y) \cos(q_k z) \tag{3}$$

where the coefficients a_{ik}, b_{ik} and nonlinear parameters $p_1, \ldots, p_N, q_1, \ldots, q_N$ are obtained by minimizing the residual RMS normal component of the total field $\mathbf{B}_{dipole} + \mathbf{B}_{cf}$ over the model magnetopause. More details on the $\mathbf{B}_{cf}$ derivation can be found elsewhere [e.g., TA15 and *Tsyganenko*, 1995, 1998a, 2002, 2013].

2.1.2. Magnetotail Field Module

The tail field is represented by a conceptually simple and algorithmically fast module, described in detail in TA15. The equatorial current is constructed by superposing 300 circular current loops of finite thickness, which overlap each other and fill the interval between the inner edge of the sheet at $R_N \sim 6-9\, R_E$ and its outer edge at $\sim 150-200\, R_E$ in the deep tail. The net magnetic field is calculated as a sum of contributions from individual loops, which lends a great deal of flexibility to the model, including the variable current sheet thickness, tail-lobe field gradient, and an easy way to deform the tail current in response to seasonal/diurnal oscillations of the geodipole tilt angle.

Combined with an appropriate shielding field, the total field of the tail module becomes confined within a prescribed model magnetopause, where the normal component $B_n \approx 0$. Adding the shielding field is effectively equivalent to redirecting the exterior part of the current sheet over the boundary in the form of theta-shaped closure currents. This important issue was discussed at length by *Sotirelis et al.* [1994] and in our review [*Tsyganenko*, 2013]; the reader is referred to those sources for more details.

The tail sheet current $I(X)$ per unit length along the X axis monotonically decreases down the tail as $I(X) = I_0(|X|/R_N)^{-\mu}$, where the coefficient I_0 and the exponent μ define, respectively, the peak intensity of the current at the sheet's inner edge (located at $X = -R_N$) and the rate of its tailward falloff. The curvature center of the tail current flow lines is shifted sunward from the origin to $X = X_c > 0$; by varying the parameter X_c one can change the amount of the inner tail current connecting to the dawn/dusk magnetopause. One more free parameter is the hinging distance R_H, which defines the magnitude of the current sheet deformation and the amplitude of its excursions from the GSM equator caused by the geodipole tilt. The magnitude of the tail current is modulated by the normalized solar wind pressure P_{dyn} via the factor $F_p = (P_{dyn}/P_0)^\zeta$ where $P_0 = 2$ nPa is the average pressure. In summary, the tail field module has six parameters, of which the first one is the magnitude coefficient A_T (proportional to the current I_0) and five nonlinear parameters are R_N, X_c, R_H, μ, and ζ.

2.1.3. Symmetric and Partial Ring Current Modules

From the physics viewpoint, the ring current is just the innermost part of the entire system of magnetospheric equatorial currents. It is formed as a result of the plasma convection and storm time injections from the tail and, as such, is unseparable from the latter. In the empirical modeling, however, the RC is treated separately, because its PRC component is asymmetric in local time and includes the Region 2 FACs which maintain the continuity of the azimuthal drift current. This is what makes the SRC/PRC different from the magnetotail field module: the tail currents are confined to a roughly planar near-equatorial sheet, which allowed us to construct it from axisymmetric circular loops and thus keep the problem effectively two-dimensional. By contrast, the presence of the FACs in the PRC system introduces the third dimension, and, as a result, we are faced with a complicated task to devise a flexible and, at the same time, a physically realistic 3-D model. The problem is somewhat mitigated by the fact that the SRC/PRC system resides in the region of rather strong quasi-dipolar magnetic field. This allows one to reconstruct, at least in a rough approximation, a 3-D configuration of the electric current and magnetic field, physically consistent with the observed distribution of equatorial plasma pressure, and then use it as a starting point to develop a practically efficient numerical model. This is just the way we chose in the past to empirically represent the inner magnetospheric field, including the latest TA15 and earlier models. As already said, all the details of the final form of the SRC/PRC module can be found in TA15 and referenced publications; in what follows below we only recapitulate the most essential points.

Based on the above scheme, our derivation of the SRC module started with defining a scalable radial distribution of the equatorial plasma, with the pressure peak in the range $3 \le r \le 4\, R_E$ and the pancake-type anisotropy steadily increasing inward, consistent with observations [e.g., *Lui and Hamilton,* 1992]. Assuming a bi-Maxwellian particle velocity distribution function and a purely dipolar background magnetic field, the corresponding plasma currents were calculated, from which the magnetic field of the model SRC was evaluated and fitted by suitable analytical functions. The next step was to apply a flexible 3-D deformation to the

obtained axisymmetric SRC field, with the goal to allow for a variable day-night asymmetry of the ring current. The deformation magnitude was treated in that procedure as a free model parameter to be fitted to magnetic field data.

The PRC field model was constructed using basically the same approach and following the same steps, except that the pressure was assumed to be isotropic, peaking at a larger radial distance ($\sim 6\,R_E$) and varying with the solar magnetic longitude ϕ as $\sin^2[(\phi - \phi_0)/2]$, where ϕ_0 is the azimuthal shift of the pressure maximum from local midnight. The Region 2 FACs associated with the azimuthally varying pressure were calculated using the current continuity equation [e.g., *Birmingham*, 1992]. As in the case of the SRC, the PRC magnetic field was initially derived using the axisymmetric purely dipolar background field, and was then subject to the same deformation, to account for the basic day-night asymmetry of the magnetosphere.

In their final form, the SRC and PRC modules were quantified by two magnitude coefficients, A_{SRC} and A_{PRC}, two variable spatial scale factors, S_{SRC} and S_{PRC}, and two parameters, ε_{SRC} and ε_{PRC}, entering in the day-night deformation function and controlling the degree of the noon-midnight asymmetry of both current systems. In addition, the PRC module also includes the rotation angle ϕ_0, parameterizing the magnetic local time (MLT) position of the PRC centroid plane.

2.1.4. Region 1 FAC Module
The global system of the Region 1 FACs is an essential part of the solar wind-magnetosphere-ionosphere system, at least in two aspects. From the physics viewpoint, it serves as a transmission line between the interplanetary medium and the ionosphere, which pumps in the solar wind energy and stirs the large-scale magnetospheric convection, eventually resulting in a wide variety of space weather phenomena. In terms of the global B field and electric current structure, the R1 FACs delineate a transition region with sheared field, separating the open high-latitude field line domain from the inner magnetosphere with a predominantly quasi-dipolar geometry.

At low altitudes, where the magnetic field is strong and dipole like, the R1 FACs are indeed field aligned, with the **j** flow lines staying in the planes of constant SM longitude. One can thus assume in a first-order approximation that the low-altitude FACs reside on a funnel-like surface, which crosses the ionosphere along the observed R1 FAC oval and expands outward in the shape of dipolar L-shells. At larger radial distances, the current flow lines no longer follow the dipolar field lines but gradually deviate toward higher latitudes, veer in the azimuthal direction, cease to be purely field aligned, and, eventually, enter/exit their generation region in the outermost magnetospheric domain and/or in the magnetosheath.

In the solar magnetic spherical coordinates $\{r, \theta, \phi\}$, the R1 FAC flow lines are modeled in the TA15 model by a set of spread-out "wires" defined by a simple equation, whose first version was introduced by *Tsyganenko and Stern* [1996] and then subsequently used in several empirical models (see TA15, section 4.4, equation (19), and references therein):

$$\sin \theta(r, \phi) = \sqrt{r} \left/ \left[r^\nu + \sin^{-2\nu} \theta_0(\phi) - 1 \right]^{1/2\nu} \right. \tag{4}$$

where the colatitude $\theta_0(\phi) = \theta_{00} + \Delta\theta_0 \sin^2(\phi/2)$ varies from θ_{00} at noon to $\theta_{00} + \Delta\theta_0$ at midnight, thus defining the size and asymmetry of the FAC oval at the ionospheric level, while the fixed parameter ν controls the shape of the FAC flow lines at large radial distances. The entire funnel-like system of the R1 FACs is represented as a superposition of multiple overlapping wires of finite thickness, with their ionospheric footpoints equidistantly spaced along the oval. The electric current strength in the wires varies with longitude as $\sin(\phi)$, which yields downward and upward currents in the dawn and dusk sectors, respectively. Equation (4) which defines the shape of the FAC wires corresponds to the case of untilted geodipole, $\psi = 0$; the dipole tilt effects are taken into account by an appropriate deformation of the entire current system, as described in more detail in TA15, [see also *Tsyganenko and Andreeva*, 2014; *Tsyganenko et al.*, 2015].

2.2. RBF Component of the Hybrid Model
In the present study, the RBF component of the hybrid model has been built on the basis of its most recent version, comprehensively described in TA16. The basic idea of the RBF approach is to decompose the magnetic field into toroidal and poloidal parts

$$\mathbf{B}(\mathbf{r}) = \nabla\Psi_t \times \mathbf{r} + \nabla \times \left(\nabla\Psi_p \times \mathbf{r} \right) \tag{5}$$

and then expand the generating scalar functions Ψ_t and Ψ_p into linear combinations

$$\Psi_t(\mathbf{r}) = \sum_{i=1}^{N} a_i\,\chi_i(|\mathbf{r} - \mathbf{R}_i|) \qquad \Psi_p(\mathbf{r}) = \sum_{i=1}^{N} b_i\,\chi_i(|\mathbf{r} - \mathbf{R}_i|) \tag{6}$$

of the radial basis functions $\chi_i(|\mathbf{r} - \mathbf{R}_i|)$, each of which depends only on the radial distance from the observation point $\mathbf{r}$ to a fixed node $\mathbf{R}_i$. Physically, the representation (5)–(6) describes the magnetic field as a sum of contributions from a set of spatially diffuse sources, more or less smoothly distributed over the entire modeling region. Each of the $2N$ terms in (6) is then split into two parts having even and odd parities with respect to the dipole tilt angle, which doubles the number of unknown coefficients. In addition, each coefficient is further expanded into a binomial of $\sqrt{P_{dyn}}$, to account for the solar wind pressure variations.

A special comment should be made here on the specific form of the RBFs. In our previous studies (AT16 and TA16), we chose $\chi_i = \sqrt{|\mathbf{r} - \mathbf{R}_i|^2 + D^2}$, where the regularization parameter $D = 4R_E$ was introduced in order to avoid singularities in the magnetic field components at $\mathbf{r} = \mathbf{R}_i$. In the course of the present work, it was found that a simpler form $\chi_i = |\mathbf{r} - \mathbf{R}_i|^3$ provided even better results. In particular, the absence of any specific scaling distance in the new RBF made the model field more regular and smooth. The ostensibly paradoxical choice of the positive exponent 3 (hence, resulting in the globally diverging RBFs) poses, in fact, no problem, owing to the multitude of the expansion terms of the same order in (6), which partially cancel each other. This interesting property of the diverging RBFs has been pointed out and duly appreciated elsewhere in the literature; the reader is referred to an excellent monograph [*Gershenfeld*, 2003, chapter 12.3] for further details.

The 3-D grid of the RBF nodes is generated by specifying first a set of nearly equidistant points on the innermost sphere of radius $R_1 = 4\,R_E$ and then replicating it radially into a nested "matryoshka-like" family of eight spheres, up to the upper distance limit of $R_8 = 18\,R_E$ (which sets the outer boundary of the model's validity region at $\sim 20\,R_E$). The total number N of the RBF nodes in this realization of the model equals 862. As explained above, each node spawns eight independent coefficients, which therefore results in 6896 unknown linear parameters to be evaluated by fitting the RBF model to the data.

To improve the RBF model performance in the case of nonzero geodipole dipole tilt angle, $\Psi \neq 0$, the originally north-south symmetric grid was allowed to deform in concert with the general tilt-induced deformation of the magnetospheric geometry, as described in detail in TA16 (section 2, Figure 1, and equations (7) and (8)) and in earlier works [e.g., *Tsyganenko and Andreeva*, 2014].

2.3. The Hybrid Fitting Procedure
Our least squares fitting code included an option to vary only a selected subgroup of the model parameters, while keeping the remaining parameters frozen at prescribed values. Following the assumed hierarchy of the model components, in the first round of calculations we fixed at zero all 6896 RBF magnitude coefficients, in order to let the principal modular component adjust itself in an optimal way to the observed magnetospheric configurations, implicitly present in the data. In the second round, the modular and RBF components changed their roles: all TA15 parameters were fixed at their best fit values obtained in the first round, while the RBF coefficients were unfixed and fitted to data, to account for the remaining discrepancies. To check the consistency of such a two-step procedure, one more pair of alternating rounds was carried out, which in all cases resulted in only a few percent further adjustment of the parameter values obtained in the first two rounds. As a measure of the relative weights of the modular and RBF components in the final solution, we calculated separate RMS magnitudes of both components in the total model field; a more detailed account of the results is given below in section 4.

3. Data and Parameterization Issues
The spacecraft data pool used in this work was essentially based on the same multiyear "grand" set of 5 min average data records with $X_{GSM} \geq -60\,R_E$, employed in TA15, AT16, and TA16. It included the data of Geotail, Polar, Cluster, Time History of Events and Macroscale Interactions during Substorms (THEMIS)-A, THEMIS-B, THEMIS-C, THEMIS-D, THEMIS-E, and Van Allen A and Van Allen B, with each record tagged by concurrent interplanetary medium data and ground-based activity indices from the OMNI database. In this work, the previously compiled set was further augmented by adding the most recent (through May 2016) data of all the above missions, except Polar (terminated in April 2008). Adding those data to the previously existing set resulted in a $\sim 13\%$ increase of its size, which raised the total number of 5 min records from 4,229,427

Table 1. Grand Data Set: Contributing Missions, Numbers of Records, and Time Spans

Mission	Number of Records	Begin Date (year/DOY)	End Date (year/DOY)
Geotail	417,285	1995/004	2016/150
Polar	873,152	1996/076	2008/108
Cluster	606,606	2001/030	2016/033
THEMIS A	600,363	2007/060	2016/152
THEMIS B	71,677	2007/060	2010/202
THEMIS C	140,444	2007/060	2010/188
THEMIS D	599,275	2007/060	2016/152
THEMIS E	614,321	2007/060	2016/152
Van Allen A	228,802	2012/252	2016/152
Van Allen B	225,404	2012/252	2016/133
Total	4,377,329		

to 4,787,362. As already noted in section 2.2, in the present study the outer nightside boundary of the modeling domain was set at $X_{\rm GSM} = -20\,R_E$, with more distant data (in particular, those of THEMIS-B and THEMIS-C taken after 2010) being excluded from the calculations. For that reason, the actual size of the grand set used in this work was somewhat smaller, with the total number of records equal to 4,377,329. More details on specific contributions to the grand data set from individual missions are given in Table 1.

The current goal of our study and the subject of the present paper are mainly to explore the principal advantages of combining the RBF and modular components into a single mathematical framework, rather than to deliver a full-scale model continuously driven by interplanetary input parameters. A detailed treatment of the parameterization issue is beyond the scope of this paper and has been deferred for a future work. Here we adopted the approach of AT16, in which the model coefficients were found for four trial subsets of the entire database, corresponding to four characteristic phases of a magnetospheric disturbance. To that end, a simple binning procedure was applied, based on the time-averaged corrected index $SYM\text{-}H_c = 0.8 \cdot SYM\text{-}H - 13\sqrt{P_{\rm dyn}}$ and its time derivative. Following a standard procedure, the 5 min average values of $SYM\text{-}H_c$ were subject to a sliding masked averaging over 2 h intervals, centered on the current time moment. Further details of the averaging procedure were described in detail in AT16 (section 3, equations (9) and (10)), and the reader is referred to that paper for more details.

Owing to the virtually gapless coverage by the $SYM\text{-}H$ index in the OMNI database, each data record in the grand set was tagged with corresponding values of the mask-averaged $\langle SYM\text{-}H_c \rangle$ and $\langle D\,SYM\text{-}H_c/Dt \rangle$. Following the approach of AT16, four data subsets were then compiled corresponding to four typical disturbance phases, defined by setting lower and upper limits on $\langle SYM\text{-}H_c \rangle$ and $\langle D\,SYM\text{-}H_c/Dt \rangle$. Figure 1, similar in format to Figure 2 of AT16, shows a diagram of the grand set data density in the 2-D space of the $\langle SYM\text{-}H_c \rangle$ and $\langle D\,SYM\text{-}H_c/Dt \rangle$ parameters. The colored rectangles delineate four ad hoc selected areas, conventionally associated with four different phases of a magnetospheric storm. Relatively small values of both the control parameters correspond to quiet conditions (Q, blue); large negative $\langle SYM\text{-}H_c \rangle$ and small $|\langle D\,SYM\text{-}H_c/Dt \rangle|$ refer to the main phase peak (M, white); large negative $\langle SYM\text{-}H_c \rangle$ and $\langle D\,SYM\text{-}H_c/Dt \rangle$ characterize the storm
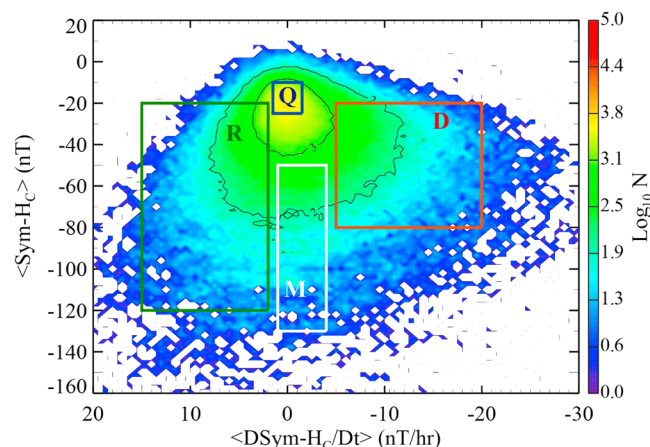

Figure 1. Diagram of the grand set data density in the $\langle SYM\text{-}H_c \rangle - \langle D\,SYM\text{-}H_c/Dt \rangle$ parameter space. The color scale corresponds to the logarithm of the number of records falling into 0.5 nT by 2 nT/h bins of the above parameters. The four colored rectangles delineate the areas corresponding to four phases of a storm according to the adopted selection criteria: the quiet prestorm state (Q, blue), the storm deepening phase (D, red), the main phase peak (M, white), and the recovery phase (R, green).

Table 2. Characteristics of the Data Subsets Corresponding to Four Storm Phases[a]

Subset Label	Number of Records	$\langle SYM\text{-}H_c \rangle$ (nT)			$\langle D\,SYM\text{-}H_c/Dt \rangle$ (nT/h)			$\langle IMF\,B_z \rangle$ (nT)	$\langle P_{dyn} \rangle$ (nPa)
		Low	High	Mean	Low	High	Mean		
Q	57,767	−25	−10	−17.6	−1.5	+1.5	+0.11	+1.56	1.57
D	51,900	−80	−20	−44.5	−20.0	−5.0	−9.32	−7.33	3.36
M	43,761	−130	−50	−66.2	−4.0	+1.0	−1.36	−4.65	2.88
R	33,216	−120	−20	−38.5	+2.0	+15.0	+4.25	+2.16	2.62

[a]The notations Q, D, M, and R stand for the quiet time, storm deepening, main, and recovery phases, respectively. Quantities in the columns include the lower and upper limits on the masked time-averaged values of the corrected *SYM-H* index and its variation rate, as well as their mean values over the subset. Last two columns list the mean values of the IMF B_z and of the solar wind ram pressure.

development (deepening) phase (D, red); and finally, negative $\langle SYM\text{-}H_c \rangle$ and positive $\langle D\,SYM\text{-}H_c/Dt \rangle$ define the recovery phase (R, green). Although similar in essence to the method of AT16, the binning procedure adopted in the present work has some significant differences. First, as already mentioned, in this study we used 2 h averaging intervals for *SYM-H$_c$* and its time derivative, instead of the 6 h intervals used in AT16, TS07, and by *Sitnov et al.* [2008]. The rationale here was to better discriminate between the storm phases, motivated by the fact that in many events the development phase (D) duration can be as short as ~2 h. Second, selection of the data into subsets was preceded by a "randomized thinning" procedure, described in detail in section 3 of TA15 and intended to at least partially level off the high disparity between the quiet time and storm time data density. Third, additional limits were imposed in three cases on the average interplanetary magnetic field (IMF) $\langle B_z \rangle$ during the 30 min preceding interval, with the purpose to more accurately distinguish between the data corresponding to different external driving conditions. Specifically, the Q and R data were required to satisfy the condition IMF $\langle B_z \rangle > 0$, while in the D case only records with $\langle B_z \rangle < -5$ nT were selected into the modeling subset. Fourth, in order to exclude from the data very unusual and extreme cases, an upper limit was imposed on the solar wind ram pressure, so that only records with $P_{dyn} \leq 20$ nPa were retained. Finally, to keep the task computationally feasible, the lower/upper limits on $\langle SYM\text{-}H_c \rangle$ and $\langle D\,SYM\text{-}H_c/Dt \rangle$ (i.e., position and size of the rectangles in Figure 1) were adjusted in such a way that the corresponding numbers of records in each subset remained within the range 30,000–60,000.

Table 2 lists the main statistical characteristics of the four data subsets, including the numbers of data records, lower and upper limits of $\langle SYM\text{-}H_c \rangle$ and $\langle D\,SYM\text{-}H_c/Dt \rangle$, and average values of IMF B_z and of the solar wind ram pressure.

4. Fitting Results

As stated in section 1, the key idea of the hybrid approach is to assign to the modular component the role of a principal contributor to the model field, while leaving it to the flexible RBF component to correct for inevitable remaining imperfections. Therefore, the first thing to check was to statistically compare the contributions of both components into the calculated model field. Table 3 lists in its first line from top the RMS values of the observed magnetic field $\left\langle \mathbf{B}_{obs}^2 \right\rangle^{1/2}$, corresponding to each of the four data subsets.

As expected, the highest (56.72 nT) and the lowest (21.00 nT) values of the RMS $\left\langle \mathbf{B}_{obs}^2 \right\rangle^{1/2}$ correspond to the M and Q subsets, respectively. We remind here in passing that both the observed and model values of the magnetic field cited throughout this work refer to only its external component (i.e., with the Earth's contribution subtracted).

The next three lines in the table show, respectively, the RMS values of the net hybrid model field $\left\langle \mathbf{B}_{hybr}^2 \right\rangle^{1/2}$ and those of its modular $\left\langle \mathbf{B}_{TA15}^2 \right\rangle^{1/2}$ and RBF $\left\langle \mathbf{B}_{rbf}^2 \right\rangle^{1/2}$ components, calculated over the corresponding data subsets. As can be seen, the relative share of the RBF component is indeed rather low, varying in the range 20–23% of $\left\langle \mathbf{B}_{hybr}^2 \right\rangle^{1/2}$, which is consistent with its assumed role as the next order correction. The next two lines display the values of the final RMS residual field $\left\langle \Delta\mathbf{B}_{hybr}^2 \right\rangle^{1/2}$ and of the "intermediate" modular RMS residual $\left\langle \Delta\mathbf{B}_{TA15}^2 \right\rangle^{1/2}$, obtained after the first round of the model fitting, during which all RBF coefficients were kept at zero. The first thing to note is that, for all four data subsets, the figure of merit expressed in terms of the ratio

Table 3. Statistical Characteristics of the Model Field Derived From the Four Data Subsets[a]

	Q	D	M	R
Hybrid Model				
$\left\langle \mathbf{B}^2_{obs} \right\rangle^{1/2}$	21.00	50.94	56.72	36.85
$\left\langle \mathbf{B}^2_{hybr} \right\rangle^{1/2}$	19.46	47.36	53.41	33.30
$\left\langle \mathbf{B}^2_{TA15} \right\rangle^{1/2}$	18.53	46.99	52.46	32.16
$\left\langle \mathbf{B}^2_{rbf} \right\rangle^{1/2}$	4.12	9.93	10.17	6.54
$\left\langle \Delta\mathbf{B}^2_{hybr} \right\rangle^{1/2}$	8.02	19.45	20.12	15.94
$\left\langle \Delta\mathbf{B}^2_{TA15} \right\rangle^{1/2}$	9.01	21.84	22.54	17.23
$R_{X,\,hybr}$	0.945	0.950	0.944	0.932
$R_{Y,\,hybr}$	0.799	0.827	0.851	0.782
$R_{Z,\,hybr}$	0.927	0.880	0.908	0.884
$R_{X,\,TA15}$	0.920	0.930	0.927	0.915
$R_{Y,\,TA15}$	0.749	0.789	0.812	0.751
$R_{Z,\,TA15}$	0.911	0.842	0.881	0.860
Pure RBF Model				
$\left\langle \Delta\mathbf{B}^2_{rbf} \right\rangle^{1/2}$	8.15	20.00	20.82	16.34
$R_{X,\,RBF}$	0.944	0.945	0.939	0.930
$R_{Y,\,RBF}$	0.768	0.804	0.827	0.739
$R_{Z,\,RBF}$	0.926	0.879	0.905	0.884

[a] $\left\langle \mathbf{B}^2_{obs} \right\rangle^{1/2}$ is the RMS of the external part of the observed field, while $\left\langle \mathbf{B}^2_{hybr} \right\rangle^{1/2}$, $\left\langle \mathbf{B}^2_{TA15} \right\rangle^{1/2}$, and $\left\langle \mathbf{B}^2_{rbf} \right\rangle^{1/2}$ refer to the full hybrid model field and its TA15 and RBF components, respectively. $\left\langle \Delta\mathbf{B}^2_{hybr} \right\rangle^{1/2}$ and $\left\langle \Delta\mathbf{B}^2_{TA15} \right\rangle^{1/2}$ are the RMS residuals, corresponding to the full hybrid model field ("hybr") and to only its TA15 component. $\{R_{X,\,hybr}, R_{Y,\,hybr}, R_{Z,\,hybr}\}$ and $\{R_{X,\,TA15}, R_{Y,\,TA15}, R_{Z,\,TA15}\}$ are the correlation coefficients between the model and observed field components, corresponding to the full hybrid model and to only its TA15 part. The lower part of the table shows the residual field and correlations, corresponding to a purely RBF model (i.e., derived without the TA15 modular component).

$\left\langle \Delta\mathbf{B}^2_{hybr} \right\rangle^{1/2} / \left\langle \mathbf{B}^2_{obs} \right\rangle^{1/2}$ varies between 36% and 43%, which is in the ballpark of typical estimates for empirical models. Second, as can be seen from comparing the values of $\left\langle \Delta\mathbf{B}^2_{hybr} \right\rangle^{1/2}$ and $\left\langle \Delta\mathbf{B}^2_{TA15} \right\rangle^{1/2}$, the effect of adding the RBF component to the modular one results in a significant improvement of the figure of merit at the second round of fitting iterations (by ~11% and ~7% for the Q/D/M and R subsets, respectively).

The next three lines show the coefficients of correlation $\{R_{X,\,hybr}, R_{Y,\,hybr}, R_{Z,\,hybr}\}$ between the observed and the hybrid model components of the magnetic field vector. The highest (~0.94–0.95) and the lowest (~0.79–0.86) correlation values were found for B_x and B_y components of the external field, respectively, while those for B_z lie somewhere between. Such an ordering is typical for all magnetospheric models (see, e.g., Figure 4 and relevant discussion in TA16) and is mostly due to the large difference in the variation range of each of the three components. For comparison, the next three lines show the corresponding values obtained for only the modular (TA15) component of the model. In all cases they are significantly (by 0.02–0.04) lower than those for the full hybrid field, which is another quantitative evidence in favor of the model improvement, achieved by combining its modular component with the RBF field.

The main question and motivation behind this study was to assess the effect of unifying the modular and RBF structures into a single model. In this regard, it is instructive to use the same four data subsets to generate four purely RBF-type models, i.e., without any contribution from a modular component, and to statistically compare the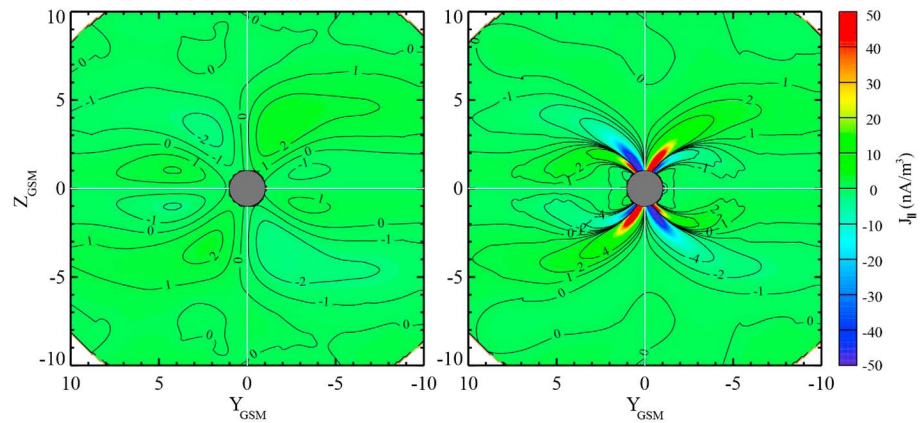 results. The lower part of Table 3 shows the outcome of such an experiment. In all four cases, the residuals $\left\langle \Delta\mathbf{B}^2_{rbf} \right\rangle^{1/2}$ for the pure RBF model were found to be tangibly (by 2–3%) higher than the corresponding values of $\left\langle \Delta\mathbf{B}^2_{hybr} \right\rangle^{1/2}$ in the upper part of the table. In terms of the correlation coefficients, the hybrid model also clearly outperforms the purely RBF model, the most significant improvement being found for the B_y component, in which case $R_{Y,\,hybr}$ is by ~0.03–0.04 larger than $R_{Y,\,RBF}$ in all four variants.

A particular cause of the improved performance of the hybrid model in the B_y component is that its modular (TA15) part provides much better representation of the low-altitude FAC effects in the innermost region $r \leq 4\,R_E$, devoid of the RBF nodes. A convincing argument in support of that conjecture is given in Figure 2 which shows two distributions of the FAC volume density in the terminator plane, calculated by taking the curl of the pure RBF model field (left) and of the hybrid model field (right). While there is a satisfactory agreement between the $J_\parallel$ distributions at $r \geq 4\,R_E$, the pure RBF model is obviously unable to represent the low-altitude part of the FACs, clearly reproduced by the modular TA15 component in the form of double red/blue tongue-like Regions 1 and 2 curtains.

An opposite example, illustrating how the RBF component of the hybrid model serves as a correction for its modular part, is given in Figure 3, comparing two meridional distributions of the scalar anomaly

Figure 2. Distributions of the FAC volume density in the plane $X_{GSM} = 0$, calculated as $(\nabla \times \mathbf{B}) \cdot \mathbf{B}/\mu_0 B$ in the pure (left) RBF model and in the (right) hybrid model. Both plots are based on the same data subset D, corresponding to the storm development phase.

$\Delta B = |\mathbf{B}_{total}| - |\mathbf{B}_{dipole}|$ with respect to the purely dipolar field. The plots in Figure 3 (left and right) correspond, respectively, to only the modular (TA15) and the full hybrid fields.

Throughout most of the modeling region both distributions look very similar, except in the outer dayside cusps, where the RBF component of the hybrid model replicates a deeper (by ~15 nT) field depression due to the penetrating magnetosheath plasma, while the TA15 component reproduces only more distant and shallower depression in the immediate vicinity of the magnetopause, corresponding to the null-point effect of the shielding. A more detailed discussion of the correction effects due to the RBF component will be given in section 5.

At this point, an important comment is in order with respect to the model magnetopause: the full hybrid field is not strictly confined within a prescribed boundary. It is merely for the reader's orientation that the color-coded distributions in Figure 3 are bounded within the *Lin et al.* [2010] model magnetopause. While in the modular component of the model each field source is separately shielded within a prescribed boundary, the situation is different for the RBF component: due to the large number of the nodes and, hence, of the expansion terms in (6), it is technically unfeasible to calculate and provide each of them with a separate individual shielding field. As a result, the net field remains incompletely shielded, so that the hybrid model cannot be used in studies focused on the boundary phenomena, in which the interconnection between the
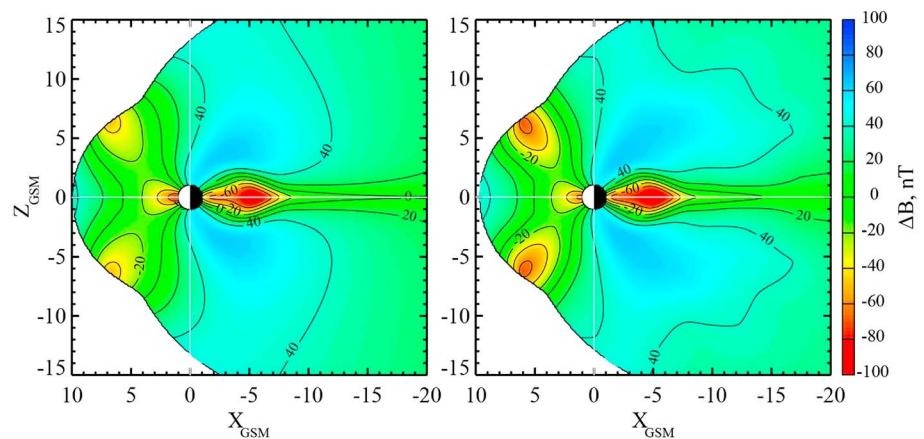

Figure 3. Distributions of the scalar anomaly $\Delta B = |\mathbf{B}_{total}| - |\mathbf{B}_{dipole}|$ with respect to the purely dipolar field, corresponding to the (right) full hybrid model and to (left) only its modular (TA15) component. The model field was calculated on the basis of the same data subset D, corresponding to the storm development phase. The plotted distributions are bounded within a *Lin et al.* [2010] model magnetopause, whose parameters (P_{dyn} and IMF B_z) were set equal to the average values for the corresponding data subset. Note a significantly deeper polar cusp depression in the case of the hybrid model.
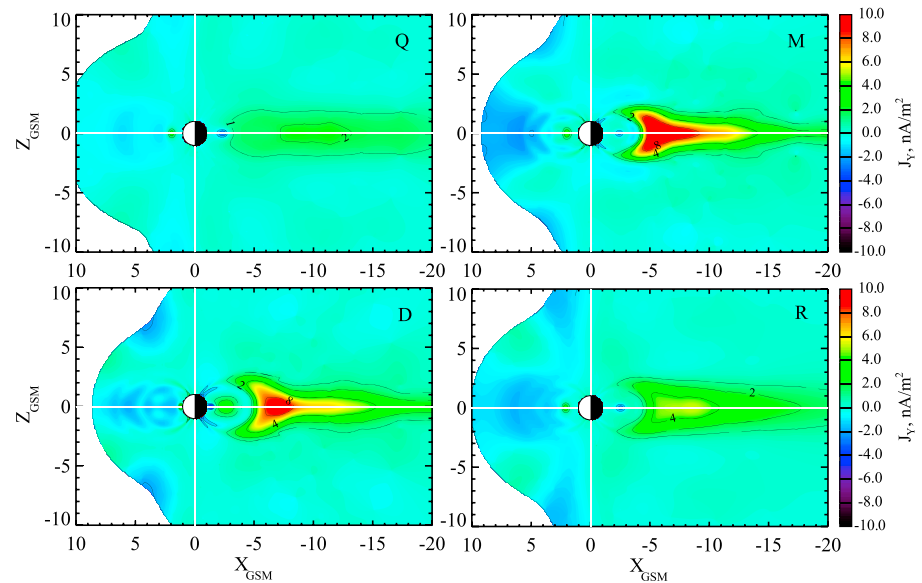
Figure 4. Meridional distributions of the dawn-dusk component J_y of the volume current density in the hybrid model, calculated as the curl of the model magnetic field vector. The four panels correspond to four states of the magnetosphere as defined via the data selection criteria, illustrated in Figure 1 and marked by letters in the upper right corner of each plot according to their nomenclature in Table 2.

magnetospheric and interplanetary fields is essential. The main goal of including the RBF component is to increase the model's flexibility in the regions densely covered by data, in particular, at low latitudes, and thereby enhance the accuracy of the field line mapping in critical areas, such as in the near-tail plasma sheet.

Figure 4 shows four meridional distributions of the dawn-dusk component J_y of the electric current volume density $\nabla \times \mathbf{B}/\mu_0$, for the quiet prestorm data (subset Q, top left), storm development phase (D, bottom left), peak of the main phase (M, top right), and storm recovery (R, bottom right). The quiet time currents are rather weak and appear as an extended and thick equatorial slab on the nightside. The storm development phase is characterized by dramatically stronger currents: on the dayside one sees a fragmented ring current at low latitudes and enhanced diamagnetic cusp currents, associated with the high-latitude field depressions (cf. Figure 3) and flowing in opposite directions at the poleward and equatorward boundaries of the cusps. On the nightside, the most outstanding feature is an intense tail current, peaking in magnitude and bifurcated into a pair of "horns" in the vicinity of its inner edge. At larger distances, $9 \leq r \leq 14\,R_E$, the current sheet becomes relatively thin and stretches tailward, with some flattening of its radial fall-off profile. A possible interpretation of this feature is a statistically averaged effect of the increase in the sunward convection of plasma during the initial phase of the storm development, accompanied with intensification and thinning of the current sheet in the near magnetotail.

The main phase peak (Figure 4, top right) is characterized by the strongest current on the nightside with the peak volume density $J_{y\,max} \approx 11\,nA/m^2$ at $r = 6.5\,R_E$ and a well-developed ring current at $r \geq 4\,R_E$ on the dayside. In the recovery phase diagram (Figure 4, bottom right), the equatorial currents decrease both on the nightside and the dayside, with a substantial flattening of the tail current profile and its overall shift to larger distances, so that in this case $J_{y\,max} \approx 5.4\,nA/m^2$ at $r = 8.4\,R_E$. On the dayside, the ring current assumes a more regular form, more closely matching the shape of the dipolar L-shells. In this case, it is also interesting to note significantly stronger diamagnetic currents on the poleward side of the cusps, probably associated with a different (tail-lobe) reconnection regime owing to the above mentioned restriction IMF $B_z > 0$, imposed in the data selection for the R subset.

5. Discussion

As noted before, the RBF component plays the role of a flexible correction to the relatively rigid modular part, and one of the goals of the present work was to test the efficiency of this method in terms of the difference between the modular and full hybrid field. In particular, it is interesting to compare the corresponding
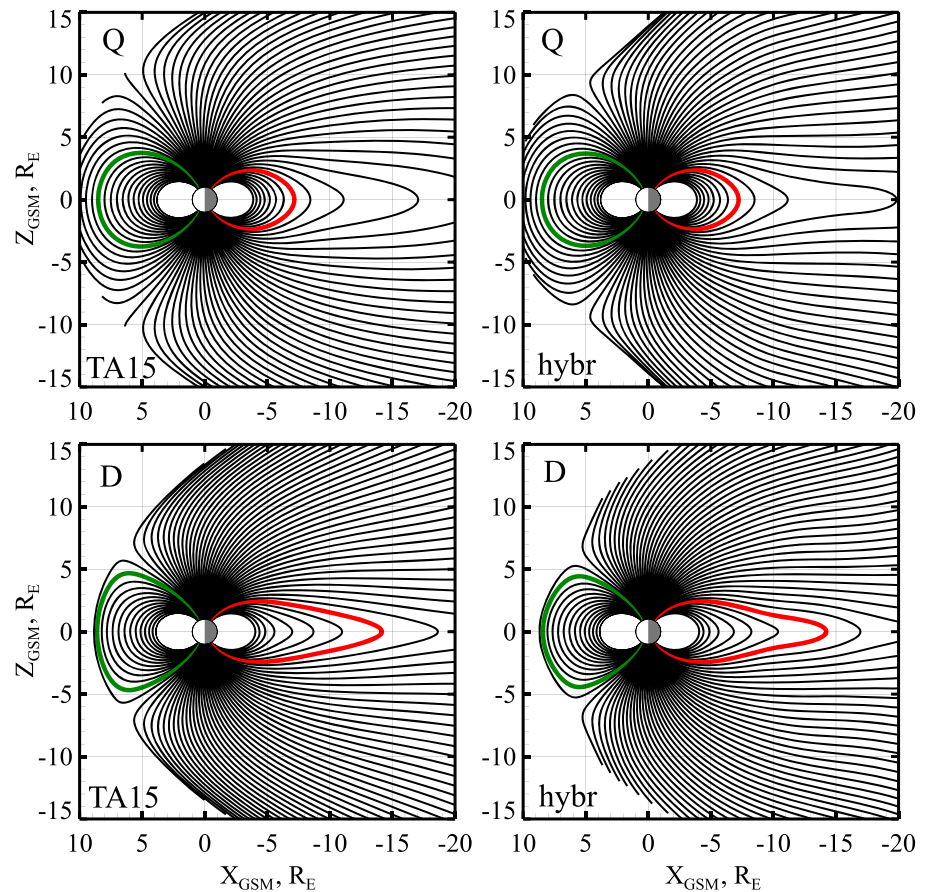
Figure 5. Noon-midnight field line configurations, calculated from (left column) only the modular (TA15) component of the model and from its (right column) full hybrid version, for the (top row) quiet prestorm (Q) and (bottom row) storm development (D) phases. The field lines follow at 1° cadence of the footpoint latitude, starting from 59° for the innermost lines. Lines with footpoint latitudes 66° at midnight and 71° at noon are highlighted with red and green, respectively.

magnetic configurations and assess the difference in the field line mapping from low altitudes to the distant magnetosphere. A set of model field line plots is presented in Figures 5 and 6. Each plot shows, side-by-side, a pair of configurations corresponding to the same data subset (Q, D, P, or R), with the modular field lines in Figures 5 and 6 (left columns) and the full hybrid field lines in Figures 5 and 6 (right columns). As can be seen from the figures, there is little difference in the corresponding low-latitude field line shapes and stretch, not exceeding a few R_E near the tailward boundary of the modeling domain at ~15 R_E. The configurations become somewhat different from each other only at high latitudes, obviously due to the scarcity or complete lack of data in that region, which results in uncontrolled deflection of the extrapolated RBF field lines. In the case of the storm development (Figure 5, bottom row) and the main phase peak (Figure 6, top row), the configurations become much more stretched on the nightside. The difference in the field line shape between the modular and full versions grows with radial distance but still does not exceed $1-2$ R_E at the outer limit of the modeling region. The polar cusps reside in both cases on the field lines with footpoints at $72-73°$, but the outermost cusp "funnel" is somewhat closer to Earth in the hybrid version, probably due to the diamagnetic depression. Also, in the hybrid model the dayside magnetopause is not as blunt as in the purely modular configuration in Figure 6 (left column). The main phase peak is characterized by even stronger nightside stretch and somewhat larger size of the dayside magnetosphere, due to a lower average solar wind pressure in the M data subset (2.88 nPa, against 3.36 nPa for the D subset).

In the case of the storm recovery (Figure 6, bottom row), the model configurations are overall much less stretched, though the outermost field lines extend substantially farther tailward in the hybrid version.
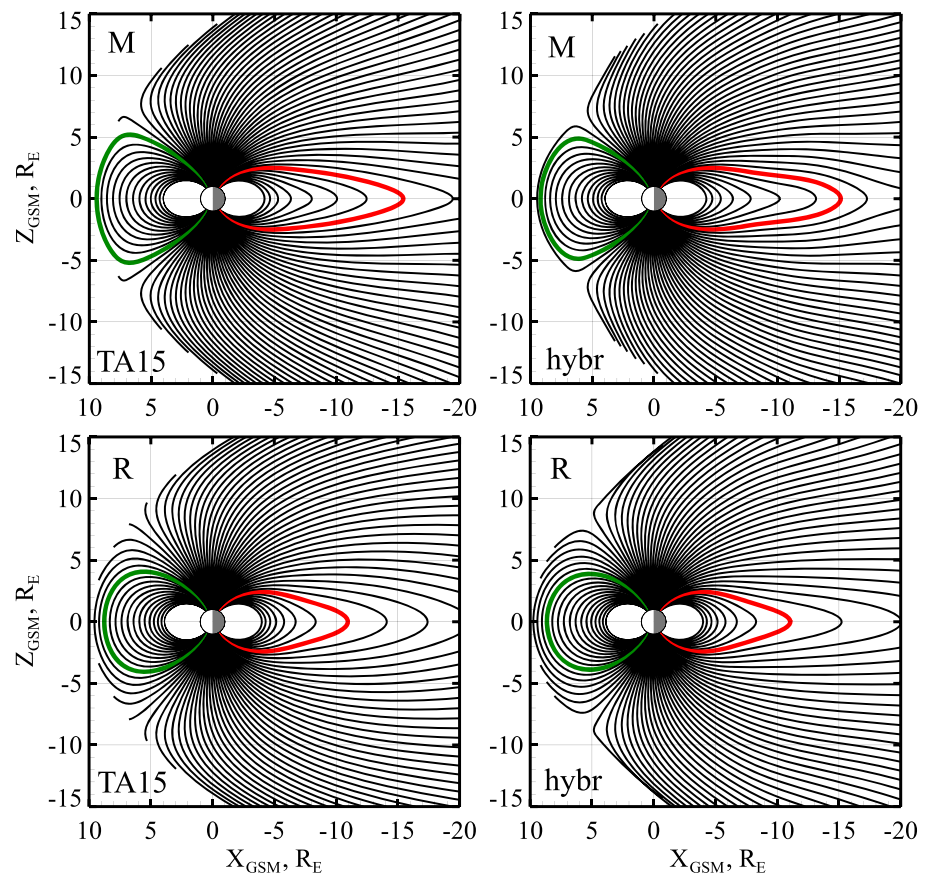
Figure 6. Same as in the previous figure but for the storm peak (M, top row) and recovery (R, bottom row) phases.

Also note a somewhat sharper reversal of the field lines across the equatorial plane in the right plot, due to a thinner current sheet in the hybrid model.

The above plotted noon-midnight configurations, however, do not provide full information on the model's mapping properties over the whole range of local time. In order to analyze that aspect in more detail, we present in Figures 7–8 plots of contours of constant solar magnetic (SM) latitude and longitude as mapped from the ground to the equatorial plane (white contours). The mapped grid (in white) is shown against the color-coded background, representing distributions of the field depression and compression in terms of the scalar anomaly with respect to the purely dipolar field $\Delta B = |\mathbf{B}_{total}| - |\mathbf{B}_{dipole}|$ (cf. Figure 3).

Figure 7 (left and right columns) corresponds, respectively, to the modular component (TA15) and to the full hybrid model (TA15+RBF). Figure 7 (top and bottom rows) displays the results obtained for the quiet (Q) and storm development (D) subsets, respectively, while the main (M) and recovery (R) phase configurations are presented in the same format in Figure 8.

The quiet time diagrams reveal a nearly dawn-dusk symmetric configuration with a weak compression on the dayside and weak depression on the nightside, with $\Delta B \sim -40$ nT at $X = -4\,R_E$ and $\Delta B \sim -20$ nT at ionospheric altitudes, in good agreement with well-known standard estimates of the ground magnetic effect of a quiet time ring current [e.g., *Langel and Estes*, 1985]. The most conspicuous difference between the full hybrid field configuration and that in the purely modular case is a significantly stronger day-night asymmetry of the innermost magnetosphere in Figure 7 (right column), such that the $\Delta B = -20$ nT contour approaches the Earth's surface in the morning sector. However, because of the very strong total field in that region, the ΔB asymmetry does not affect the mapping geometry there. At larger distances, one sees only a slight dawn-dusk asymmetry, which may well be due to some nonuniformity of data distribution.

The plots look completely different in the next case of a disturbed model field corresponding to the storm deepening phase (D), shown in Figure 7 (bottom row). Here besides the generally larger depression
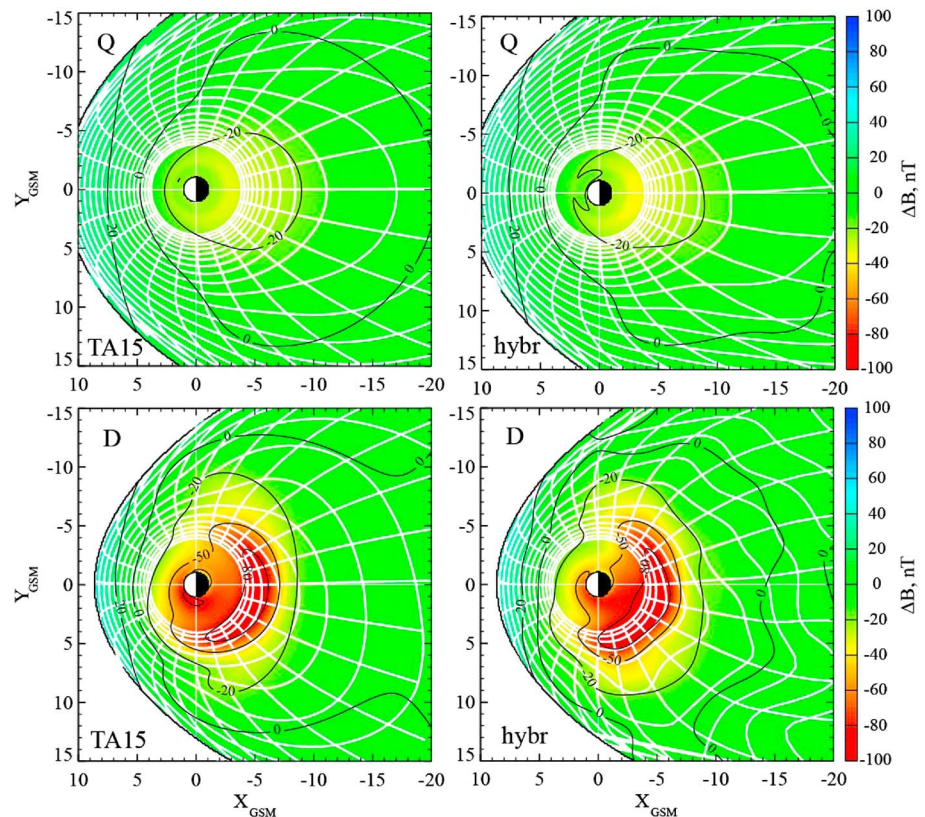
Figure 7. Illustrates mapping properties of the obtained model fields in terms of contours of constant SM latitude and longitude, mapped from low altitudes to the equatorial plane along the model magnetic field lines. The contours are plotted in white, with 1° and 6° cadence of the footpoint latitude and longitude, respectively, and the innermost latitude circles correspond to the footpoint latitude of 59°. The color background and black equal intensity contours show distributions of the scalar anomaly $\Delta B = |\mathbf{B}_{total}| - |\mathbf{B}_{dipole}|$. (left and right columns) Only the modular (TA15) component and the full hybrid field. The results obtained for the (top row) prestorm quiet time and (bottom row) storm development phases, derived from the Q and D data subsets.

and compression, there is a severe dawn-dusk asymmetry in the entire inner magnetosphere, penetrating down to ionospheric altitudes. The field depression is much deeper in the dusk sector, in agreement with a vast body of evidence, both from direct observations and previous modeling studies [e.g., *Le et al.*, 2004, and reference therein].

There is again a notable difference between the left and right columns of Figure 7: adding the RBF component to the modular part results in a significant modification of the innermost ΔB pattern, resulting in further increase of the dawn-dusk asymmetry at low altitudes and on the ground. Also, in the full hybrid case the contours of equal ΔB are much more irregular and wavy, which is due to several factors: first of all, a highly nonuniform and patchy data distribution in the geometric and parametric space, as well as a much more dynamic near-tail field.

The next pair of plots (Figure 8, top row) presents the diagrams corresponding to the subset M for the storm main phase, which reveal further deepening of the inner field depression and its farther expansion to the dayside. However, the dawn-dusk asymmetry is not as dramatic as in the preceding plots of Figure 7, due to the longitudinal propagation of the depressed field area, which is especially pronounced in the left column corresponding to only the modular TA15 component. Adding the RBF component results, on the one hand, in a larger longitudinal nonuniformity of ΔB and, on the other hand, in a more circular depressed field area, readily seen in the shape of the isointensity line $\Delta B = -20$ nT. As in the previous case, note the increasingly wavy and irregular contour shapes at larger tailward distances.

Finally, in Figure 8 (bottom row) a pair of diagrams is presented corresponding to the recovery phase. Here both the depression and its dawn-dusk asymmetry get weaker. Also (as in the quiet time diagram in Figure 7)
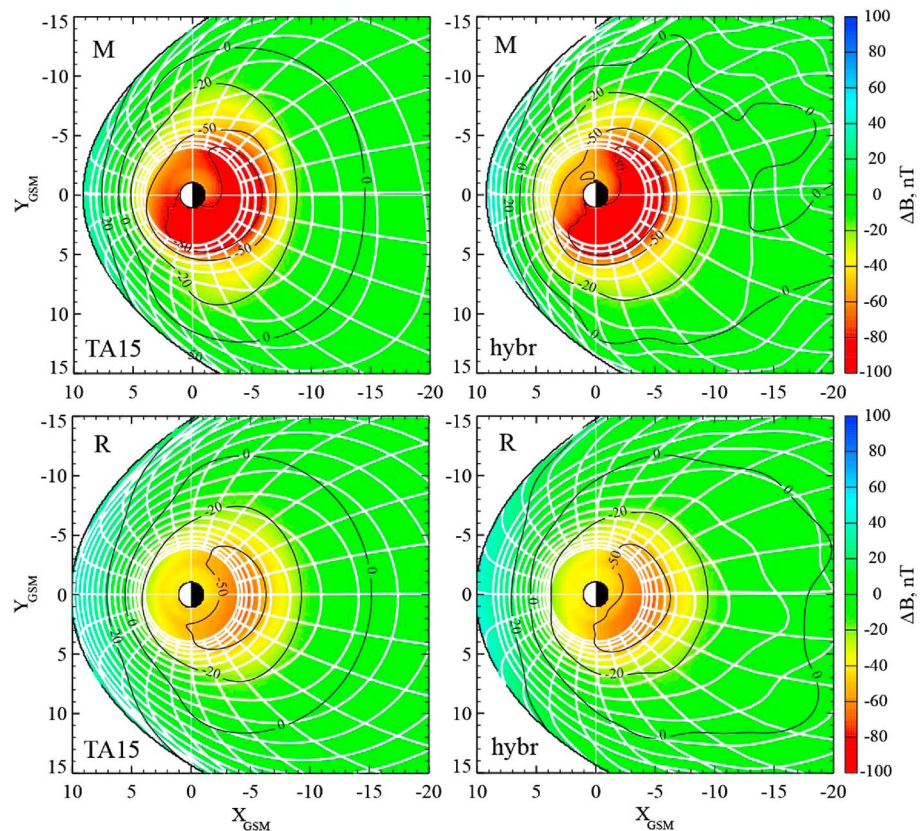
Figure 8. Same as in Figure 7 but for the storm peak (M, top row) and recovery (R, bottom row).

note a significantly more regular shape of both ΔB and mapped latitude/longitude grid contours, in comparison with those in the storm time D and M plots. This conclusively indicates the large variability of the storm time magnetosphere as a principal cause of the irregular structure of the hybrid model field.

An illustrative way to visualize and estimate the relative contribution of the RBF component to the net model field at different locations is to calculate and plot diagrams of the differential scalar anomaly $\delta\Delta B = \Delta B_{hybr} - \Delta B_{TA15}$, where $\Delta B_{hybr} = |\mathbf{B}_{hybr}| - |\mathbf{B}_{dipole}|$ and $\Delta B_{TA15} = |\mathbf{B}_{TA15}| - |\mathbf{B}_{dipole}|$. Figure 9 displays four meridional distributions of $\delta\Delta B$, calculated for the same four states of the magnetosphere, annotated by the corresponding letters in the left top corners of each diagram.

The most outstanding feature in all four diagrams is the area of pronounced field depression in the polar cusps. Unlike in a similar plot in Figure 3, the diagrams in Figure 9 no longer contain the vacuum part of the depression represented by the TA15 component (now subtracted) but reveal the separate effect of the diamagnetic currents inside the cusps. This is demonstrated in an especially dramatic way in Figure 9 (top right), corresponding to the storm peak phase (M), where the added depression penetrates all the way down to Earth.

Another interesting difference of this diagram from all other ones is an outstanding compression of the magnetic field in the immediate vicinity of the dayside magnetopause. A possible interpretation here is that while both the M and D subsets have a significantly elevated average wind ram pressure (2.9 and 3.4 nPa, respectively), the D phase is characterized in addition by fast loading and strong external driving due to a large and negative IMF B_z. This is why the $\delta\Delta B$ in the D panel (Figure 9, bottom left) is slightly negative, reflecting the strong reconnection and penetration of the southward IMF B_z. By contrast, the M case corresponds on the average to much weaker loading rate and, hence, larger subsolar fields, which is reflected in the diagram as the dark blue layer near the subsolar magnetopause.

A persistent feature in all the diagrams in Figure 9 is vast regions adjacent to the high-latitude tail magnetopause, where the lobe field is by a few nanotesla weaker than predicted by the TA15 model. The most likely interpretation of that depression is a highly dynamical shape and size of the disturbed magnetopause.
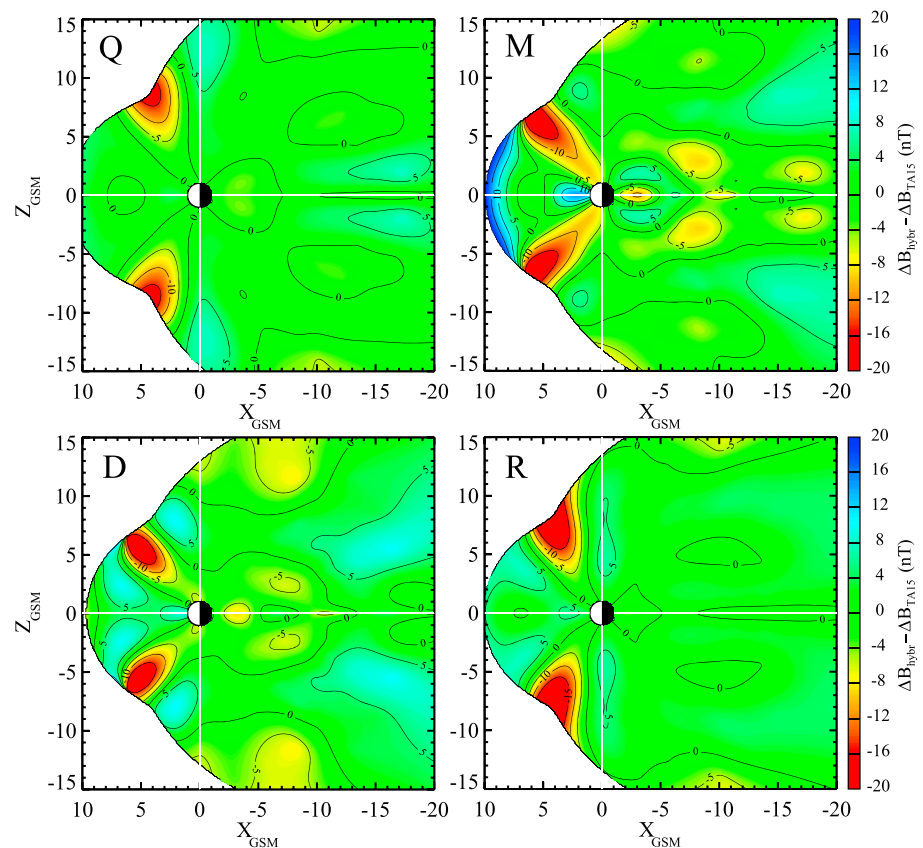
Figure 9. Meridional distributions of the differential scalar anomaly $\delta\Delta B = \Delta B_{\text{hybr}} - \Delta B_{\text{TA15}}$ for four magnetospheric states, illustrating the contribution of the RBF model component in the total hybrid field in terms of the magnetic field compression (blue) and depression (red).

Combined with intermittent penetration of plasma mantle particles during active periods, that may effectively result in a reduced tail lobe field. Such an explanation is consistent with the fact that the yellow areas of depressed B in the above plots expand in size in the D and M diagrams.

6. Summary and Outlook

In this paper we proposed and presented the results of testing a new approach to construct the magnetosphere magnetic field models based on space magnetometer data. The essence of the method is to combine a standard empirical model, built from a few dedicated modules, with the recently developed RBF representation of the magnetic field, composed as a sum of toroidal/poloidal parts, with their generating potentials being expanded into sums of the radial basis functions. The work is motivated by the fact that, on the one hand, the standard modular models are inevitably limited in their flexibility, due to a number of preconceived notions on the magnetospheric field source geometry. On the other hand, the new RBF approach developed in AT16 and TA16, in spite of its great flexibility, yields good results only in the regions densely covered with observations but is prone to uncontrolled diverging field patterns away from those areas. Hence, our expectation was that using a globally regular and stable modular structure as a principal component and adding the RBF part as a flexible correction would result in a trade-off solution, combining in a single model the strengths of both approaches and minimizing their individual weaknesses. As shown above, the suggested fitting procedure indeed maintains the expected hierarchy between the modular and RBF components and yields consistent results, in terms of both spatial configuration of the model field and its restructuring during magnetospheric disturbances. Based on this, we believe that the suggested synthetic approach is worthwhile and can be utilized in future empirical modeling projects, in which sufficient spatial resolution will be of primary importance. In particular, it can play a principal role in the development of a modeling tool to reconstruct in real-time instantaneous geospace magnetic configurations, based on simultaneous data flow from

a host of small satellites [e.g., *Tsyganenko* [1998b], and other articles in that volume]. Another important and persistently challenging aspect for the future work is the model parameterization. In the present study we did not venture in that area but limited ourselves with testing the hybrid approach on four trial data subsets. At least two parameterization methods can be envisioned here. The first one is based on "best universal" driving functions, incorporating information on both current and past state of the solar wind-magnetosphere system [*Tsyganenko and Sitnov*, 2005]. The second method employs the "nearest-neighbor" data selection, taking full advantage of tremendous amount of information on the magnetospheric response to the interplanetary input, hidden in multiyear data archives [*Sitnov et al.*, 2008; *Stephens et al.*, 2013, 2016].

References

Andreeva, V. A., and N. A. Tsyganenko (2016), Reconstructing the magnetosphere from data using radial basis functions, *J. Geophys. Res. Space Physics*, *121*, 2249–2263, doi:10.1002/2015JA022242.

Birmingham, T. J. (1992), Birkeland currents in an anisotropic, magnetostatic plasma, *J. Geophys. Res.*, *97*(A4), 3907–3917.

Farrell, W. M., and J. A. Van Allen (1990), Observations of the Earth's polar cleft at large radial distances with the Hawkeye 1 magnetometer, *J. Geophys. Res.*, *95*, 20,945–20,958.

Fairfield, D. H. (1991), An evaluation of the Tsyganenko magnetic field model, *J. Geophys. Res.*, *96*(A2), 1481–1494.

Gershenfeld, N (2003), *The Nature of Mathematical Modeling*, Cambridge Univ. Press, Cambridge.

Langel, R. A., and R. H. Estes (1985), Large-scale, near-field magnetic fields from external sources and the corresponding induced internal field, *J. Geophys. Res.*, *90*(B3), 2487–2494.

Le, G., C. T. Russell, and K. Takahashi (2004), Morphology of the ring current derived from magnetic field observations, *Ann. Geophys.*, *22*, 1267–1295.

Lin, R. L., X. X. Zhang, S. Q. Liu, Y. L. Wang, and J. C. Gong (2010), A three-dimensional asymmetric magnetopause model, *J. Geophys. Res.*, *115*, A04207, doi:10.1029/2009JA014235.

Lui, A. T. Y., and D. C. Hamilton (1992), Radial profiles of quiet time magnetospheric parameters, *J. Geophys. Res.*, *97*, 19,325–19,332.

Sitnov, M. I., N. A. Tsyganenko, A. Y. Ukhorskiy, and P. C. Brandt (2008), Dynamical data-based modeling of the stormtime geomagnetic field with enhanced spatial resolution, *J. Geophys. Res.*, *113*, A07218, doi:10.1029/2007JA013003.

Sotirelis, T., N. A. Tsyganenko, and D. P. Stern (1994), Method for confining the magnetic field of the cross-tail current inside the magnetopause, *J. Geophys. Res.*, *99*, 19,393–19,402.

Stephens, G. K., M. I. Sitnov, J. Kissinger, N. A. Tsyganenko, R. L. McPherron, H. Korth, and B. J. Anderson (2013), Empirical reconstruction of storm time steady magnetospheric convection events, *J. Geophys. Res. Space Physics*, *118*, 6434–6456, doi:10.1002/jgra.50592.

Stephens, G. K., M. I. Sitnov, A. Y. Ukhorskiy, E. C. Roelof, N. A. Tsyganenko, and G. Le (2016), Empirical modeling of the storm time innermost magnetosphere using Van Allen Probes and THEMIS data: Eastward and banana currents, *J. Geophys. Res. Space Physics*, *121*, 157–170, doi:10.1002/2015JA021700.

Tsyganenko, N. A. (1995), Modeling the Earth's magnetospheric magnetic field, confined within a realistic magnetopause, *J. Geophys. Res.*, *100*, 5599–5612.

Tsyganenko, N. A. (1998a), Modeling of twisted/warped magnetospheric configurations using the general deformation method, *J. Geophys. Res.*, *103*(A10), 23,551–23,563.

Tsyganenko, N. A. (1998b), Toward real-time magnetospheric mapping based on multi-probe space magnetometer data, in *Science Closure and Enabling Technologies for Constellation Class Missions*, edited by V. Angelopoulos and P. V. Panetta, pp. 84–90, UCLA, Berkeley, Calif.

Tsyganenko, N. A. (2002), A model of the near magnetosphere with a dawn-dusk asymmetry: 1. Mathematical structure, *J. Geophys. Res.*, *107*(A8), 1179, doi:10.1029/2001JA000219.

Tsyganenko, N. A. (2009), Magnetic field and electric currents in the vicinity of polar cusps as inferred from Polar and Cluster data, *Ann. Geophys.*, *27*, 1573–1582, doi:10.5194/angeo-27-1573-2009.

Tsyganenko, N. A. (2013), Data-based modelling of the EarthŠs dynamic magnetosphere: A review, *Ann. Geophys.*, *31*, 1745–1772, doi:10.5194/angeo-31-1745-2013.

Tsyganenko, N. A., and V. A. Andreeva (2014), On the "bowl-shaped" deformation of planetary equatorial current sheets, *Geophys. Res. Lett.*, *41*, 1079–1084, doi:10.1002/2014GL059295.

Tsyganenko, N. A., and V. A. Andreeva (2015), A forecasting model of the magnetosphere driven by an optimal solar wind coupling function, *J. Geophys. Res. Space Physics*, *120*, 8401–8425, doi:10.1002/2015JA021641.

Tsyganenko, N. A., and V. A. Andreeva (2016), An empirical RBF model of the magnetosphere parameterized by interplanetary and ground-based drivers, *J. Geophys. Res. Space Physics*, *121*, 10,786–10,802, doi:10.1002/2016JA023217.

Tsyganenko, N. A., and D. P. Stern (1996), Modeling the global magnetic field of the large-scale Birkeland current systems, *J. Geophys. Res.*, *101*(A12), 27,187–27,198.

Tsyganenko, N. A., and C. T. Russell (1999), Magnetic signatures of the distant polar cusps: Observations by Polar and quantitative modeling, *J. Geophys. Res.*, *104*(A11), 24,939–24,955.

Tsyganenko, N. A., and M. I. Sitnov (2005), Modeling the dynamics of the inner magnetosphere during strong geomagnetic storms, *J. Geophys. Res.*, *110*, A03208, doi:doi:10.1029/2004JA010798.

Tsyganenko, N. A., V. A. Andreeva, and E. I. Gordeev (2015), Internally and externally induced deformations of the magnetospheric equatorial current as inferred from spacecraft data, *Ann. Geophys.*, *33*, 1–11, doi:10.5194/angeo-33-1-2015.